APPENDICES

Appendix A. Thermobarometry of magmatic andalusite.

Appendix B. SHRIMP-RG analytical procedures, U-Pb geochronology, zircon characterization and trace-element geochemistry.

Appendix C. Trace-element geochemistry results.

Appendix D. $^{40}Ar/^{39}Ar$ step heating analytical procedures.

Figure A1. (a) Subhedral, single andalusite crystal interstitial to plagioclase and quartz, partly replaced by muscovite. Photomicrograph with crossed polarizers. (b) Andalusite, sillimanite, and muscovite along a leucogranite micro-shear band. Andalusite is randomly oriented (different grey scales in image), and rimmed by oriented sillimanite and muscovite. Photomicrograph with crossed polarizers. (c) Temperature and pressure locations of experimentally-determined stability fields for aluminum silicate polymorphs and wet granite solidi curves. Solidi are from Scaillet et al. (1995) and from Holtz et al. (2001); aluminum silicate stability fields are from Richardson et al. (1969) (R 69), Holdaway (1971) (H 71), and Pattison (1992) (P 92). The light grey field outlines the estimated maximum stability field for andalusite in our samples. The dark grey field highlights the estimated pressure for the crystallization and re-equilibration of muscovite along shear bands (after Masonne and Schreyer, 1987). The black field shows the most probable pressure and temperature conditions for muscovite formation and re-equilibration. The star marks the estimated conditions for the final crystallization of leucogranite BH 225.

Figure B1. Zircon characterization. (a) and (f) are imaged by cathodoluminescence (CL) only, while for (b)-(e), back-scattered electron images are on the left and CL images of the same grains are on the right. Dashed circles denote spots for U-Pb analyses while dotted circles denote spots for both U-Pb and Ti-in-zircon analyses.

Appendix A: Thermobarometry of magmatic andalusite

Andalusite makes up to ≤3 vol % of BH 225, forming ≤1 mm large, subhedral to euhedral single crystals, or clusters of crystals that are ~50-1000 μm large, anhedral to subhedral, and randomly oriented (Fig. A1a). Most andalusite grains display concentric or sector zoning, are inclusion-free and are partially replaced by sillimanite and muscovite. Andalusite occurs in interstitial spaces between phenocrysts, along grain boundaries, or as marginal inclusions in zoned magmatic plagioclase and cordierite. Similar andalusite has previously been described from Miocene leucogranites of the Everest-Makalu region (e.g., Searle, 1999; Visonà and Lombardo, 2002). The andalusite- and sillimanite-bearing leucogranites of the Everest-Makalu region have been interpreted as peritectic magmatic minerals and possibly as restite crystals (Visonà and Lombardo, 2002).

The presence of andalusite in BH 225 therefore indicates that the leucogranite crystallized at low pressures. The maximum P-T-X stability for andalusite remains controversial, given difficulties to constrain the exact locations of the andalusite–sillimanite field boundary and the position of the granite solidus for specific compositional systems (e.g., Clarke et al., 2004). Assuming the water-saturated granite solidi of Scaillet et al. (1995) or Holtz et al. (2001), and the andalusite–sillimanite stability field proposed by Richardson (1969), andalusite may crystallize at a pressure as high as ca. 4.8-5.2 kbar at 630-650 °C. Assuming the andalusite–sillimanite stability field proposed by Pattison (1992), which has found support in most recent studies (e.g., Cesare

et al., 2003; Johnson et al., 2003; Wei et al., 2007), andalusite may have its maximum stability at only 2.6-3.0 kbar at 640-660 °C.

For BH 225, we suggest that andalusite crystallized close to or at the solidus (given its interstitial occurrence), and therefore at a pressure of probably ≤2.8 kbar (medium grey field, Fig. A1c), or at maximum ≤5.0 kbar (light grey field, Fig. A1c).

Evidence for significant deformation during magmatic evolution is lacking. The rock fabrics discussed above indicate that the leucogranites were deformed at sub-solidus conditions. Locally developed shear bands host muscovite and fibrolitic sillimanite, which partly rim magmatic andalusite. To crystallize sillimanite following andalusite, pressure or temperature must have increased, or the composition of the system must have changed in a way that reduced the andalusite stability to lower temperatures or pressures (e.g., by reducing Mn or Fe^{3+} concentrations; Grambling and Williams, 1985). A pressure increase seems unlikely since all thermobarometric studies to date suggest continuous decompression for the GHS at that time (e.g., Hollister and Grujic, 2006 and references therein). On the other hand, a small, short-term temperature increase and/or compositional modification of the system during high-temperature, sub-solidus deformation, seem both probable. Hot fluids, liberated from large granite intrusions may have facilitated deformation, and percolated along the shear bands, permitting the crystallization of sillimanite over magmatic andalusite.

References

Cesare, B., Marchesi, C., Hermann, J., and Gomez-Pugnaire, M. T., 2003, Primary melt inclusions in andalusite from anatectic graphitic metapelites: Implications for the position of the Al2SiO5 triple point: Geology, v. 31, p. 573-576.

Clarke, D.B., Dorais, M., Barbarin, B., Barker, D., Cesare, B., Clarke, G., El Baghdad,

M., Erdmann, S., Förster, H.-J., Gaeta, M., Gottesmann, B., Jamieson, R.A., Kontak, D.J., Koller, F., Gomes, C.L., London, D., Morgan, G.B., Neves, L.J.P.F., Pattison, D.R.M., Pereira, A.J.S.C., Pichavanti, M., Rapela, C.W., Renno, A.D., Richards, S., Roberts, M., Rottura, A., Saavedra, J., Sial, A.N., Toselli, A.J., Ugidos, J.M., Uher, P., Villaseca, C., Visonà, D., Whitney, D.L., Williamson, B., and Woodard, H.H., 2005, Occurrence and origin of andalusite in peraluminous felsic igneous rocks: Journal of Petrology, v. 46, p. 441-472.

Grambling, J.A., and Williams, M.L., 1985, The effects of Fe^{3+} and Mn^{3+} on aluminum silicate phase relations in north-central New Mexico, U.S.A.: Journal of Petrology, v. 26(2), p. 324-354.

Hollister, L.S., and Grujic, D., 2006, Pulsed channel flow in Bhutan, *in* Channel Flow, Ductile Extrusion, and Exhumation in Continental Collision Zones, Law, R., Searle, M.P., and Godin, L., Geological Society, London, Special Publications, v. 268 p. 415-423.

Holtz, F., Becker, A., Freise, M., and Johannes, W., 2001, The water-undersaturated and dry Qz-Ab-Or system revisited. Experimental results at very low water activities and geological implications: Contributions to Mineralogy and Petrology: v. 141(3), p. 347-357.

Johnson, T. E., Brown, M., and Solar, G. S., 2003, Low-pressure subsolidus and suprasolidus phase equilibria in the MnNCKFMASH system: Constraints on conditions of regional metamorphism in western Maine, northern Appalachians: American Mineralogist, v. 88(4), p. 624-638.

Masonne, H.-J., and Schreyer, W., 1987, Phengite geobarometry based on the limiting assemblage with K-feldspar, phlogopite, and quartz, Contributions to Mineralogy and Petrology, v. 96, p. 212-224.

Pattison, D. R. M., 1992, Stability of andalusite and sillimanite and the Al_2SiO_5 triple point: constraints from the Ballachulish aureole, Scotland: Journal of Geology, v. 100, p. 423–446.

Richardson, S. W., Gilbert, M. C., and Bell, P. M., 1969, Experimental determination of kyanite-andalusite and andalusite-sillimanite equilibria; the aluminum silicate triple point: American Journal of Science: v. 267(3), p. 259.

Searle, M. P., 1999, Extensional and compressional faults in the Everest-Lhotse Massif, Khumbu Himalaya, Nepal: Journal of the Geological Society, v. 156(2), p. 227-240.

Scaillet, B., Pichavant, M., and Roux, J., 1995, Experimental Crystallization of Leucogranite Magmas: Journal of Petrology, v. 36(3), p. 663-705.

Visonà, D., and Lombardo, B., 2002, Two-mica and tourmaline leucogranites from the Everest-Makalu region (Nepal-Tibet). Himalayan leucogranite genesis by isobaric heating?: Lithos, v. 62, p. 125-150.

Wei, C., Clarke, G., Tian, W., and Qiu, L., 2007, Transition of metamorphic series from the Kyanite-to andalusite-types in the Altai orogen, Xinjiang, China: Evidence from petrography and calculated KMnFMASH and KFMASH phase relations: Lithos, v. 96(3-4), p. 353-374.

Appendix B. SHRIMP-RG analytical procedures, U-Pb geochronology and trace element geochemistry, and zircon characterization

Analytical procedures

Minerals, concentrated by standard heavy mineral separation processes and hand picked for final purity, were mounted on double-stick tape on glass slides in 1 x 6 mm rows, cast in epoxy, ground and polished to a 1 micron finish on a 25 mm diameter by 4 mm thick disc. All grains were imaged with transmitted light and reflected light (and incident light if needed) on a petrographic microscope, and with cathodoluminescence and back scattered electrons (for older zircons) as needed on a JEOL 5600 SEM to identify internal structure, inclusions and physical defects. Fractures observed in the zircons during imaging are likely a result of the separation process (crushing and milling) since the least fractured grains are found in sample BH 225, which was separated by Selfrag. The fractures also coincide with porous areas of the zircon grains, which are likely weaker zones. The mounted grains were washed with 1N HCl or EDTA solution (if acid soluble) and distilled water, dried in a vacuum oven, and coated with Au. Mounts typically sat in a loading chamber at high pressure (10-7 torr) for several hours before being moved into the source chamber of the SHRIMP-RG. Secondary ions were generated from the target spot with an O_2^- primary ion beam varying from 4-6 nA. The primary ion beam produced a spot with a diameter of 20-40 microns and a depth of 1-2 microns for an analysis time of 9-12 minutes. Nine peaks were measured sequentially for zircons (the SHRIMP-RG is limited to a single collector, usually an EDP electron multiplier): $^{90}Zr_2{}^{16}O$, ^{204}Pb, Bgd (0.050 mass units above ^{204}Pb), ^{206}Pb, ^{207}Pb, ^{208}Pb, ^{238}U,

$^{248}Th^{16}O$, $^{254}U^{16}O$. Autocentering on selected peaks and guide peaks for low or variable abundance peaks (i.e. $^{96}Zr^{216}O$ 0.165 mass unit below ^{204}Pb) were used to improve the reliability of locating peak centers. The number of scans through the mass sequence and counting times on each peak were varied according to sample age and U and Th concentrations to improve counting statistics and age precision. Measurements were made at mass resolutions of 6000-8000 (10% peak height) which eliminated all interfering atomic species. The SHRIMP-RG was designed to provide higher mass resolution than the standard forward geometry of the SHRIMP I and II (Clement and Compston, 1994). This design also provides very clean backgrounds and combined with the high mass resolution, the acid washing of the mount, and rastering the primary beam for 90-120 seconds over the area to analyzed before data is collected, assures that any counts found at mass ^{204}Pb are actually Pb from the zircon and not surface contamination. In practice greater than 95% of the spots analyzed have no common Pb. Concentration data for zircons are standardized against zircon standard R33 (419 Ma, quartz diorite of Braintree complex, Vermont, John Aleinikoff, pers. comm.) which are analyzed repeatedly throughout the duration of the analytical session. Data reduction follows the methods described by Williams (1997) and Ireland and Williams (2003) and uses the Squid and Isoplot programs of Ken Ludwig. Between U-Pb analyses and Ti-in-zircon analyses the zircon mounts were repolished and recoated with gold.

Zircon characterization

Zircons were imaged under cathodoluminescence (CL) and back-scattered electrons (BSE) using a JEOL scanning electron microscope (Fig. A1; Hanchar and

Miller, 1993). The five samples collected from leucogranites within the hanging wall of the lower STD share many characteristics. Sample DBH 003 zircons are small (50-200 m along long axis), while the other grains range from 150-500 m. Some grains display both terminations, but many are fractured, possibly by crushing during sample preparation due to the porous structure of many of the grains. DBH 003 and DBH 036 yielded a few zircons with distinctive bright xenocrystic cores rimmed by either thick, sector-zoned, dark under CL (low U) rims (i.e., Fig. A1a, grains 11 and 14) or by zircon with a mottled texture (i.e., Fig. A1a, grains 8 and 9). However, most of the grains lack xenocrystic cores and the interiors of the zircons are mottled, containing numerous holes and inclusions, while their concentrically-zoned igneous-type rims are typically free of holes and inclusions (see BSE images, Fig. A1b) (run a few grains in the microprobe to determine mineralogy of the inclusions). In sample DBH 031 zoned rims are typically observed only at pyramid terminations, not along the prism faces, and there are thin, bright under CL (low U) rims ringing some crystals, perhaps indicating late local recrystallization (Corfu et al., 2003; see CL images, Fig. A1c). Sample DBH 036 zircons generally exhibit thick (≤50 m thick), concentrically-zoned rims (Fig. A1d) and grain interiors composed of mottled zircon with holes and inclusions (Fig. A1d grain 3), except for one grain that has a more complex internal texture of zonation (Fig. A1d grain 10). DBH 080 zircons rims are only locally concentrically-zoned. Grain interiors have the mottled texture, with abundant inclusions and holes, although some sections also appear cloudy and dark under CL (e.g., Fig. A1e).

There are at least three texturally-distinct growth phases present in the zircons described above. Bright xenocrystic cores in DBH 003 and the zoned core in DBH 036

are probably relicts from protoliths. All samples (with the exception of DBH 003) contain zircons with concentrically zoned rims, although growth zoning is only locally observed in DBH 080. Oscillatory rims are widely described as in the literature as magmatic. Here the oscillatory, concentrically zoned rims likely grew during crystallization of the leucogranites. The dark (under CL, light under BSE) color of both the rims and the mottled texture indicates the generally high U content of the zircons (Rubatto and Gebauer, 2000). The origin of the mottled zircon texture, which comprises a significant component of almost all zircon grains, is uncertain. It has been observed elsewhere in zircons from leucogranites derived from partial melting and crystallization under low P/low T conditions (Booth et al., 2004). A locally observed faint oscillatory zonation (e.g., Fig. 4a grain 8) and young intermediate ages (between detrital core and magmatic rim ages) suggest sub-solidus recrystallization. However, the texture is not one typically observed in recrystallized zircons (i.e., Rubatto and Gebauer, 2000). It could possibly be a product of a highly fractionated, trace element-rich early partial melt. The high U content, abundant holes and inclusions and uncertain origin of the mottled zircon texture make it difficult to interpret U-Pb results from this phase. Thus, they will not be considered further, and interpretation of U-Pb ages will be confined to the cores and rims, although results from mottled zircon are included in the data tables. Thin bright rims found surrounding some zircon crystals (e.g., Fig. A1c grain 5) may reflect another growth phase but as these rims are too thin to sample, their ages cannot be determined.

BH 225 zircons are texturally distinct from the lower STD zircons described above, and contain from two to four distinct growth phases. In general, cores display a range of sector zoning (Fig. A1f grain 65), concentric zoning (Fig. A1f grain 25), or more

complex convoluted zoning (Fig. A1f grain 53), suggesting a sedimentary protolith (Rubatto and Gebauer, 2000). Cores are often embayed and surrounded by grey-under-CL zircon with weak or no concentric zoning (i.e., Fig. A1f grain 2) and then rimmed by zircon that is concentrically zoned and dark under CL. The grey-under-CL zircon may be magmatic or metamorphic. Dating of this texture yielded detrital ages, mixed ages and ages coincident with dark rims. Again, the dark, oscillatory-zoned rims are likely magmatic in origin, crystallizing in the leucogranite. The mottled texture ubiquitous to zircons found in the lower STD is not observed in this sample, and the grains are relatively free of holes and inclusions, except for isolated large inclusions of ? commonly observed in the cores (i.e., Fig. A1f grain 59).

Trace element geochemistry of mottled zircon

The trace element geochemistry of mottled zircon is similar to that of the zircon rims. Most of the mottled zircons display a small positive Ce anomaly, and a large negative Eu anomaly. Mottled zircon from sample DBH 003 is variable and distinct from the other samples, ranging from a small positive to a small negative Ce anomaly, a small to no Eu anomaly and an abundance of light rare earth elements (LREEs). This variability in trace element geochemistry may indicate contamination by inclusions, a different protolith source, or that it is not an analogous growth phase to the mottled zircon in the other four samples.

References

Bickford, M.E., Cullers, R.L., Shuster, R.d., Premo, W.R., and VanSchmus, W.R., 1989, U-Pb zircon geochronology of Proterozoic and Cambrian plutons in the Wet

Mountains and southern Front Range, Colorado: Geological Society of America Special Paper 235, p. 33-48.

Black,L.P, Kamo, S.L., Allen, C.M, Davis, D.W., Aleinikoff, J.N., Mundil, R., Campbell, I.H., Korsch, R.J., Williams, I.S., and Foudoulis, C., 2004, Improved $^{206}Pb/^{238}U$ microprobe geochronology by monitoring of trace-element-related matrix effect; SHRIMP, ID-TIMS, ELA-ICP-MS and oxygen isotope documentation for a series of zircon standards: Chemical Geology, v. 205, p. 115-140.

Booth, A. L., Zeitler, P. K., Kidd, W. S. F., Wooden, J., Liu, Y., Idleman, B., Hren, M., and Chamberlain, C. P., 2004, U-Pb zircon constraints on the tectonic evolution of southeastern Tibet, Namche Barwa area: American Journal of Science, v. 304, no. 10, p. 889.

Clement, S.W.J., and Compston, W., 1994, Ion probe parameters for very high resolution without loss of sensitivity, U.S. Geological Survey Circular 1107, p. 62.

Hanchar, J. M., and C. F. Miller, 1993, Zircon zonation patterns as revealed by cathodoluminescence and backscattered electron images: implications for interpretation of complex crustal histories: Chemical geology, v. 110(1-3), p. 1-13.

Ireland, T.R. and Williams, I.S., 2003, Considerations in zircon geochronology by SIMS, Zircon: in Reviews in Mineralogy and Geochemistry, edited by J.M. Hanchar and Hoskins, P.W.O., v. 53, p. 215-241.

Ludwig, K.R., 2001, Squid, A users manual: Berkeley Geochronology Center Special Publication No. 2.

Ludwig, K.R., 2003, Isoplot 3.00, a geochronological toolkit for Excel, Berkeley Geochronology Center Special Publication No. 4.

Paces, J.B., and Miller, J.D., 1993, U-Pb ages of the Duluth Complex and related mafic intrusions, northeastern Minnesota: geochronologic insights into physical, paleomagnetic and tectonomagmatic processes associated with the 1.1 Ga mid-continent rift system: Journal of Geophysical Research, v. 98, p. 13,997-14,013.

Rubatto, D., and Gebauer, D., 2000, Use of cathodoluminescence for U-Pb zircon dating by ion microprobe: some examples from the Western Alps: Cathodoluminescence in Geosciences, p. 373–400.

Williams, I.S., 1997, U-Th-Pb geochronology by ion microprobe: not just ages but histories: Society of Economic Geologists Reviews in Economic Geology, v. 7, p. 1-35.

Appendix C. Chondrite-normalized trace element values for zircon used to plot trace element patterns. Chondrite-normalizing values are from McDonough and Sun (1995). For sample labels: bold=rims, regular=mottled, italics=cores, grey=BH 225 grey interior, grey fill=anomalous REE pattern (not plotted in Fig. 5).

	La	Ce	Pr§	Nd	Sm	Eu	Gd	Tb	Dy	Ho	Er	Tm	Yb	Lu	$(Sm/La)_N$	Ce/Ce*	Hf (ppm)	Eu/Eu*	Th/U	$(Yb/Gd)_N$
DBH 003																				
1.1	389.482	120.69	112.39	60.38	68.90	98.18	127.8		519		1078		4085		0.2	0.48	9883	0.9981	1.0804	31.95
10.1	125.919	39.50	31.29	15.60	14.59	9.99	47.5		285		822		2686		0.1	0.50	9482	0.3217	0.0662	56.53
11.1	1.604	2.28	1.04	0.83	15.34	5.81	194.3		877		1853		2610		9.6	1.73	10657	0.0554	0.0132	13.44
11.2	0.365	17.42	0.79	1.15	8.64	3.27	54.8		188		507		870		23.7	30.28	9639	0.1030	0.4191	15.88
12.1	7.853	12.36	10.34	11.87	73.51	21.30	466.3		2358		5270		12948		9.4	1.36	10930	0.0789	0.0984	27.77
14.1R	11.726	12.33	5.51	3.78	36.41	16.75	333.5		964		1639		1966		3.1	1.43	10560	0.0906	0.0359	5.89
14.2C	0.192	46.13	0.91	1.96	18.37	16.26	158.4		493		1196		1432		95.4	84.04	10139	0.1840	0.3564	9.04
2.1	25.505	6.19	10.62	6.86	25.35	5.49	118.5		432		1123		3093		1.0	0.34	10572	0.0763	0.0229	26.10
3.1	2.376	2.08	1.51	1.20	5.69	1.43	31.5		301		1168		4816		2.4	1.07	10936	0.0771	0.1996	152.80
4.1	4.100	5.64	2.97	2.52	17.31	7.11	149.1		816		1713		2812		4.2	1.60	10066	0.0855	0.0344	18.86
5.1	1.171	1.34	0.75	0.60	8.53	1.10	92.6		512		1106		1639		7.3	1.40	8964	0.0218	0.0200	17.70
5.2C	2707.946	2181.95	1251.61	850.91	763.80	74.59	762.6		637		1323		3071		0.3	1.10	10176	0.0977	0.8441	4.03
6.1	2.321	3.28	1.50	1.21	15.53	5.27	203.0		1489		3509		6106		6.7	1.72	9257	0.0482	0.0136	30.08
7.1	19.366	26.37	18.18	17.62	61.30	6.76	170.4		686		2164		8895		3.2	1.40	10209	0.0583	1.0569	52.21
8.1	6.192	14.98	4.42	3.73	9.14	4.88	48.0		205		677		1684		1.5	2.82	10352	0.1709	0.1399	35.11
9.1	85.020	18.04	32.79	20.36	36.71	18.02	92.9		375		1047		3998		0.4	0.31	10202	0.2782	0.6898	43.04
9.2	13.704	39.94	8.35	6.51	36.82	14.87	189.0		460		1069		1623		2.7	3.62	10023	0.1317	0.7047	8.59
DBH 027																				
2.2	0.000	0.57	0.00	0.25	9.39	1.35	171.7	717	1119	1047	1055	1130	1120	762			29951	0.0336	0.0040	5.40
A4.1	0.028	0.37	0.07	0.10	4.99	1.14	89.9	389	653	697	714	836	881	721	180	8.5	27945	0.0540	0.0031	8.11
A2.1	0.073	0.43	0.13	0.17	5.10	0.35	65.2	266	428	503	456	537	594	599	70	4.5	30434	0.0193	0.0073	7.53
6.1	1.655	1.05	0.53	0.30	8.31	1.60	149.9	622	1029	1033	1127	1377	1590	1237	5	1.1	27586	0.0452	0.0039	8.78
2.1	0.020	0.53	0.08	0.16	4.68	0.72	78.8	348	571	626	678	824	884	751	236	13.3	26530	0.0372	0.0033	9.29
14.1	0.864	1.47	1.24	1.48	14.71	1.76	155.9	603	1045	1112	1288	1534	1652	1193	17	1.4	22503	0.0368	0.0044	8.78
17.1	3.281	1.77	0.58	0.24	3.63	0.85	49.5	200	359	414	426	510	572	465	1	1.3	23236	0.0632	0.0033	9.57
1.1	0.087	0.64	0.09	0.10	4.53	0.57	83.8	368	602	649	679	901	979	899	52	7.1	27452	0.0294	0.0035	9.67
14.3	0.020	0.61	0.11	0.25	7.86	1.35	128.2	517	937	1089	1315	1717	1910	1585	397	13.1	20227	0.0426	0.0044	12.33
19.2	0.046	0.37	0.08	0.10	2.53	0.45	46.9	202	360	435	523	710	794	780	54	6.1	36031	0.0417	0.0042	14.02
A11.1	0.039	0.58	0.09	0.14	3.59	0.55	48.7	197	371	439	585	808	919	926	91	9.7	23904	0.0420	0.0037	15.62
20.1	0.219	0.55	0.21	0.20	1.84	0.49	25.7	114	225	299	384	517	569	557	8	2.6	21937	0.0713	0.0024	18.31
15.1	0.082	0.45	0.07	0.06	2.54	0.42	34.9	152	294	420	504	703	795	725	31	5.9	19454	0.0449	0.0029	18.83
1.2	0.048	0.42	0.08	0.10	2.04	0.32	34.7	131	258	340	446	611	700	660	42	6.9	20351	0.0384	0.0020	16.69
A11.2	0.127	0.52	0.13	0.14	2.50	1.42	39.2	187	356	459	583	808	983	1000	20	4.0	23356	0.1438	0.0035	20.74
19.1	0.365	1.04	0.39	0.41	3.19	4.26	35.4	146	289	406	491	670	815	756	9	2.7	21630	0.4008	0.0430	19.05
A4.2	0.086	0.48	0.06	0.05	1.85	0.44	28.4	130	245	319	426	596	733	703	21	6.8	19821	0.0612	0.0026	21.35
A3.1	0.124	0.63	0.30	0.46	6.20	0.68	66.8	262	450	570	711	1079	1419	1501	50	3.3	20022	0.0336	0.0042	17.60
5.1	0.046	0.40	0.10	0.14	1.68	0.33	28.9	139	280	398	528	742	938	889	36	6.0	28530	0.0479	0.0084	26.88

	La	Ce	Pr§	Nd	Sm	Eu	Gd	Tb	Dy	Ho	Er	Tm	Yb	Lu	$(Sm/La)_N$	Ce/Ce*	Hf (ppm)	Eu/Eu*	Th/U	$(Yb/Gd)_N$
A12.1	0.037	0.40	0.05	0.07	1.89	0.29	31.5	150	290	394	580	792	1103	1187	50	8.8	24196	0.0375	0.0031	29.02
A1.2	0.044	0.34	0.08	0.12	2.34	0.64	44.5	162	350	547	784	1179	1551	1653	53	5.6	24905	0.0627	0.0033	28.84
A1.1	0.119	0.31	0.07	0.05	2.14	0.46	29.5	150	312	479	746	1099	1497	1602	18	3.5	26923	0.0576	0.0035	42.03
9.1	2.880	1.77	0.68	0.33	3.33	1.23	29.8	151	362	581	906	1431	1909	2010	1	1.3	33052	0.1239	0.0066	52.95
11.1	7.206	4.40	0.86	0.30	2.64	2.42	39.1	164	352	539	883	1539	2228	2649	0	1.8	26639	0.2378	0.0061	47.16
A5.1	0.393	0.62	0.21	0.16	1.36	0.85	20.8	89	196	346	550	954	1347	1640	3	2.2	19341	0.1600	0.0033	53.70
DBH 031																				
10.1	0.646	1.77	0.16	0.08	1.31	0.04	12.2		97		192		452		2.0	5.56	39797	0.0099	0.0813	30.60
10.2	0.622	1.63	0.33	0.24	2.69	0.14	22.1		135		267		797		4.3	3.60	41103	0.0186	0.0531	29.88
12.1	1.727	2.05	0.62	0.37	2.41	0.12	17.8		127		321		1114		1.4	1.99	37752	0.0186	0.0294	51.94
15.1	0.385	1.55	0.22	0.16	1.50	0.11	10.8		94		218		753		3.9	5.34	40906	0.0274	0.0349	57.46
15.2	1.029	2.01	1.08	1.11	15.06	0.19	84.8		291		414		1078		14.6	1.90	37345	0.0052	0.0197	10.52
16.1	2.444	2.43	0.52	0.24	1.48	1.23	12.3		99		170		381		0.6	2.15	35934	0.2882	0.0710	25.61
2.1	2.223	2.37	1.38	1.08	21.25	0.46	171.3		657		649		1226		9.6	1.35	44530	0.0076	0.0197	5.93
25.1	933.958	253.89	97.24	31.38	30.83	2.68	69.3		232		325		812		0.0	0.84	32084	0.0580	0.0436	9.70
28.1	7.949	4.88	2.57	1.46	3.94	0.13	20.8		125		259		924		0.5	1.08	36231	0.0141	0.0157	36.80
3.1	3.009	3.27	3.16	3.24	45.55	0.55	217.7		704		844		2139		15.1	1.06	39145	0.0055	0.0518	8.13
4.1	0.217	1.14	0.07	0.04	0.64	0.15	7.0		65		193		615		2.9	9.40	39042	0.0709	0.0679	72.25
5.1	1.378	1.65	1.30	1.26	24.60	0.20	135.5		417		558		1339		17.8	1.24	30773	0.0035	0.0133	8.18
8.1	0.828	1.23	0.90	0.93	15.60	0.06	93.0		317		367		1063		18.8	1.43	52046	0.0017	0.0177	9.45
9.1	3.585	5.32	6.13	8.02	109.62	0.76	488.4		1356		1347		2976		30.6	1.13	52762	0.0033	0.0253	5.04
31.1	1.280	2.43	2.38	3.24	53.59	0.32	227.9		484		559		1395		41.9	1.39	50529	0.0029	0.0273	5.07
DBH 036																				
1.1	0.024	0.40	0.06	0.09	4.41	0.13	61.3	288	516	554	744	1192	1635	1529	183	10.6	37510	0.0080	0.0140	22.09
2.1	0.907	2.39	1.23	1.44	20.66	0.17	134.6	409	635	675	928	1420	1757	1584	23	2.3	35156	0.0033	0.0227	10.81
3.1	0.077	0.58	0.10	0.11	2.67	0.22	35.0	182	413	625	1108	2131	3331	3771	35	6.7	34198	0.0225	0.0218	78.71
4.1	0.047	0.31	0.09	0.12	2.53	0.14	36.1	142	278	387	568	886	1173	1251	53	4.9	21826	0.0146	0.0052	26.88
5.2	0.837	1.77	1.22	1.48	7.21	0.99	67.6	204	397	503	1228	2405	4213	5441	9	1.8	26119	0.0449	0.0135	51.58
6.1	0.009	0.42	0.03	0.05	3.38	0.02	39.6	193	364	410	613	941	1401	1380	360	25.9	33052	0.0021	0.0091	29.27
8.1	1.292	0.66	0.21	0.08	2.40	0.19	25.9	119	230	314	436	684	914	973	2	1.3	31504	0.0241	0.0065	29.28
9.1	0.574	0.95	0.60	0.62	5.88	0.40	47.9	176	312	463	608	982	1370	1557	10	1.6	27037	0.0240	0.0101	23.69
10.1	0.000	0.60	0.00	0.07	1.84	1.05	23.3	72	102	99	96	105	110	94			19487	0.1599	0.0112	3.90
11.1	0.449	0.85	0.43	0.42	7.08	0.16	94.6	401	647	677	764	987	1108	1029	16	1.9	27565	0.0063	0.0061	9.70
13.1	0.230	0.98	0.56	0.87	15.63	1.39	205.4	749	1481	2096	3262	4719	6010	6162	68	2.7	22659	0.0246	0.0065	24.22
14.1	0.052	0.53	0.11	0.15	2.92	0.02	49.6	239	446	535	728	1202	1790	1763	56	7.1	35533	0.0019	0.0104	29.89
15.1	2.634	1.62	0.60	0.28	5.42	0.75	70.6	256	498	697	1066	1706	2405	2748	2	1.3	24614	0.0385	0.0054	28.17
16.1	0.731	3.67	1.06	1.27	17.24	0.05	145.5	451	602	608	721	1095	1425	1252	24	4.2	64358	0.0009	0.0195	8.10
19.1	1.160	0.83	0.29	0.14	2.11	0.09	25.6	114	232	307	454	749	1074	1162	2	1.4	30010	0.0123	0.0073	34.71
20.1	0.842	1.16	0.48	0.36	4.07	1.28	89.1	354	643	736	1189	1715	2286	2353	5	1.8	22349	0.0672	0.0093	21.25
25.1	0.120	0.54	0.12	0.12	2.11	0.10	31.8	111	168	151	180	237	284	246	18	4.5	41626	0.0126	0.0132	7.39
28.1	0.714	0.82	0.29	0.18	2.77	0.22	40.3	192	386	514	699	1030	1335	1371	4	1.8	30983	0.0211	0.0097	27.41
DBH 080																				
1.1	0.049	0.43	0.09	0.11	5.09	0.12	59.6	131	100	54	34	43	34	33	104	6.6	39934	0.0070	0.0092	0.57
	La	**Ce**	**Pr§**	**Nd**	**Sm**	**Eu**	**Gd**	**Tb**	**Dy**	**Ho**	**Er**	**Tm**	**Yb**	**Lu**	**$(Sm/La)_N$**	**Ce/Ce***	**Hf**	**Eu/Eu***	**Th/U**	**$(Yb/Gd)_N$**

																	(ppm)			
2.1	0.049	0.45	0.07	0.08	2.75	0.13	38.3	144	187	136	138	184	241	223	57	7.8	31209	0.0129	0.0062	6.29
2.3	2.352	9.82	8.40	15.87	109.28	0.53	207.0	395	365	260	250	337	421	388	46	2.2	31501	0.0035	0.0326	2.03
5.1	0.078	0.40	0.14	0.18	4.35	0.14	77.9	220	196	113	90	102	98	92	56	3.9	30621	0.0078	0.0062	1.26
5.3	0.954	3.30	2.70	4.53	32.61	0.30	80.6	169	133	83	63	71	82	78	34	2.1	33775	0.0058	0.0364	1.02
9.2	0.050	0.36	0.11	0.15	4.48	0.13	45.4	133	138	95	80	86	92	69	90	4.9	39748	0.0093	0.0067	2.02
14.1	0.098	0.49	0.09	0.09	3.07	0.15	39.2	136	151	102	94	130	145	140	31	5.1	31375	0.0135	0.0062	3.69
15.1	0.060	0.31	0.07	0.08	4.16	0.09	47.2	114	94	47	36	34	32	32	69	4.8	36431	0.0068	0.0072	0.69
17.1	0.040	0.29	0.06	0.08	5.10	0.06	59.8	136	128	94	93	134	184	170	126	5.9	42314	0.0033	0.0119	3.07
22.1	0.048	0.46	0.06	0.06	2.77	0.13	40.4	130	136	94	97	116	145	127	57	8.7	33397	0.0127	0.0062	3.58
22.2	0.053	0.42	0.07	0.09	3.21	0.13	50.6	139	127	75	65	75	83	75	60	6.7	30122	0.0103	0.0060	1.65
25.1	0.055	0.32	0.05	0.05	3.13	0.09	42.3	114	97	56	42	41	48	48	57	6.0	31983	0.0081	0.0052	1.14
27.1	0.057	0.34	0.05	0.05	2.74	0.09	49.1	140	133	76	60	74	80	72	48	6.3	31088	0.0074	0.0055	1.64
1.2	0.631	1.78	1.49	2.28	32.03	0.31	213.8	558	658	520	449	513	537	447	51	1.8	29568	0.0038	0.0091	2.51
2.2	0.384	1.07	0.87	1.30	16.07	0.07	81.4	190	222	190	240	388	536	542	42	1.9	28591	0.0019	0.0050	6.59
2.2B	0.329	1.07	0.72	1.07	14.69	0.04	124.9	338	390	284	295	389	468	411	45	2.2	31463	0.0010	0.0110	3.74
5.2	0.802	1.48	1.80	2.71	28.16	0.29	126.8	303	395	447	656	1257	1961	2340	35	1.2	29555	0.0048	0.0278	15.47
9.1	0.579	1.71	1.27	1.88	47.41	0.30	396.6	827	675	381	259	222	196	124	82	2.0	46375	0.0022	0.0286	0.49
11.1	0.230	0.72	0.35	0.44	11.53	0.07	128.0	298	274	161	127	119	123	86	50	2.5	28716	0.0017	0.0106	0.96
12.1	0.180	0.56	0.22	0.24	5.15	0.07	55.4	154	184	136	151	209	262	268	29	2.8	30968	0.0039	0.0115	4.74
16	0.020	1.08	0.08	0.17	16.55	0.15	214.7	620	611	366	266	260	227	158	814	26.1	73091	0.0025	0.0244	1.06
16.2	0.903	0.83	0.71	0.63	15.46	0.50	177.0		292	140	86	75	61	41	17	1.0	48045	0.0095	0.0236	0.35
BH 225																				
13.1DRK	0.033	0.75	0.20	0.47	9.21	1.58	137.7	431	964	1912	3312	4831	6057	6641	275	9.25	15301	0.0443	0.0262	36.40
15.1DKR	0.066	7.68	0.36	0.85	17.57	4.41	204.6	561	1084	2062	3400	4659	5786	6424	266	49.59	14889	0.0736	0.1320	23.41
2.1DKR	0.171	0.96	0.44	0.70	14.48	3.10	197.7	548	1188	2264	3891	5659	7094	7506	85	3.52	16422	0.0580	0.0328	29.71
21.2GInt	0.016	0.25	0.03	0.04	1.04	0.15	10.8	42	109	234	492	1002	1694	2274	63	10.88	16876	0.0462	0.0020	129.87
22.1GR	0.553	1.56	0.61	0.64	11.14	2.73	144.2	463	996	1903	3164	4694	5837	6441	20	2.68	15658	0.0682	0.0329	33.50
23.1DKR	0.034	1.20	0.24	0.65	10.88	2.09	132.4	479	984	1966	3429	5320	7293	8726	316	13.11	14810	0.0552	0.0105	45.59
23.2GInt	0.044	0.76	0.15	0.27	6.92	1.90	90.8	275	566	1043	1725	2432	3096	3749	157	9.48	14472	0.0759	0.0154	28.22
25.3DRK	0.010	0.65	0.13	0.46	9.26	1.66	123.7	369	801	1577	2721	4052	4996	5240	926	18.10	15955	0.0490	0.0238	33.43
27.1DRK	0.036	0.90	0.23	0.59	12.06	2.44	170.8	528	1233	2394	4218	6157	7770	8364	339	9.95	15439	0.0538	0.0255	37.64
3.1DKR	0.022	7.30	0.24	0.78	14.05	4.26	247.4	684	1506	2989	5005	7079	9073	10206	644	101.50	12331	0.0723	0.1202	30.36
3.2GInt	0.094	0.72	0.11	0.12	1.13	1.01	14.3	31	57	90	124	165	185	230	12	7.04	12019	0.2527	0.0884	10.67
30.2GInt	0.149	7.23	1.46	4.57	34.14	17.64	216.7	405	640	1067	1501	1908	2197	2467	229	15.50	9202	0.2051	0.8866	8.39
34.1DKR	0.168	1.06	0.31	0.42	7.50	1.39	109.2	361	816	1594	2685	3991	5125	5805	45	4.66	17087	0.0485	0.0172	38.86
35.1DKR	0.083	1.04	0.41	0.90	10.25	1.85	134.7	420	907	1760	3048	4413	5704	6158	124	5.65	16179	0.0498	0.0228	35.04
35.3GInt	0.023	0.20	0.03	0.03	0.27	0.15	0.4	3	9	29	98	226	504	919	12	7.74	13428	0.4527	0.0298	1068.39
39.1DKR	0.049	1.23	0.28	0.67	12.45	3.02	172.9	525	1130	2065	3618	5121	6431	6891	252	10.43	16249	0.0651	0.0335	30.78
42.2DKR	4.332	3.34	1.38	0.77	4.95	1.08	61.1	209	455	759	1384	2515	3954	4660	1	1.37	20590	0.0620	0.0038	53.58
43.1DKR	0.135	0.59	0.28	0.40	9.61	2.02	144.6	471	1080	2144	3698	5397	6795	7545	71	3.07	15565	0.0541	0.0282	38.91
46.1DKR	0.010	9.55	0.26	1.30	21.68	4.93	282.5	745	1415	2697	4528	6328	8048	9039	2168	188.71	13165	0.0630	0.1365	23.58
49.1DKR	0.349	1.19	0.52	0.64	12.49	2.43	155.4	472	1008	1935	3329	4858	5954	6514	36	2.78	16896	0.0551	0.0274	31.72
5.1DKR	0.046	0.62	0.12	0.20	6.49	1.00	87.5	306	713	1442	2606	3919	4939	5577	142	8.35	16320	0.0420	0.0159	46.74
65.1DKR	6.403	5.25	1.76	0.92	7.51	2.13	94.4	305	717	1335	2504	4029	5664	6509	1	1.56	20678	0.0799	0.0117	49.68

§ Calculated from Anders and Grevesse (1989). * Calculated, not measured. N subscript denotes that values were chondrite-normalized before calculation.

References

Anders, E., and Grevesse, N., 1989, Abundances of the elements- Meteoritic and solar: Geochimica et Cosmochimica Acta, v. 53(1), p. 198-200.

McDonough, W. F., and Sun, S., 1995, The composition of the Earth: Chemical Geology, v. 120(3-4), p. 223-253.

Appendix D. $^{40}Ar/^{39}Ar$ step heating analytical procedures

We followed the principles and method of of $^{40}Ar/^{39}Ar$ dating described in McDougall and Harrison (1988). Coarse, pristine muscovite grains were hand picked from material crushed by a jaw crusher. The separated mica concentrates were individually wrapped in aluminum foil, and then stacked in an aluminum irradiation canister. Interspersed among the samples were five to seven aliquots of the flux monitor, Fish Canyon tuff sanidine, which has an apparent K-Ar age of 28.205 ± 0.046 Ma (Kuiper et al. 2008). The canister was irradiated with fast neutrons in the nuclear reactor at McMaster University in Hamilton, Ontario, Canada. At Dalhousie University, a double-vacuum tantalum resistance furnace was used to carry out the step-heating. Isotopic analyses were made in a VG3600 mass spectrometer using both Faraday and electron multiplier collectors to measure the abundance of ^{39}Ar for $^{40}Ar/^{39}Ar$ and $^{36}Ar/^{39}Ar$ ratios, respectively. Errors are reported at the 2σ level and include the uncertainty in the irradiation parameter, J, but do not incorporate uncertainty in the assumed age of the flux monitor.

References

Kuiper, K.F., Deino, A., Hilgen, F.J.,Krijgsman, W.,Renne, P.R., and Wijbrans, J.R., 2008, Synchronizing rock clocks of Earth history, Science, v. 320, p. 500-504.

MacDougall, I., and Harrison, T.M., 1988, Geochronology and thermochronology by the $^{40}Ar/^{39}Ar$ method: Oxford University Press, New York, 212 p.

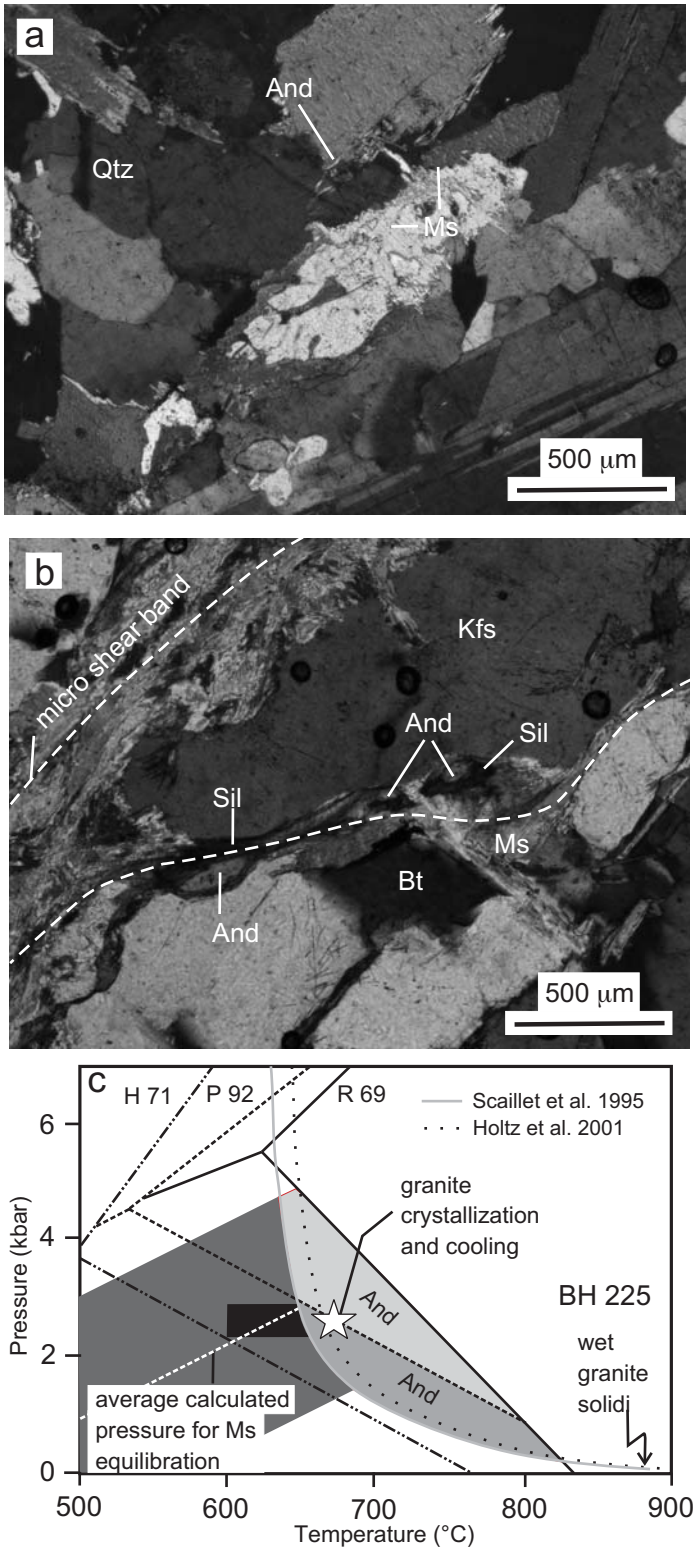

Figure A1, Kellett et al.

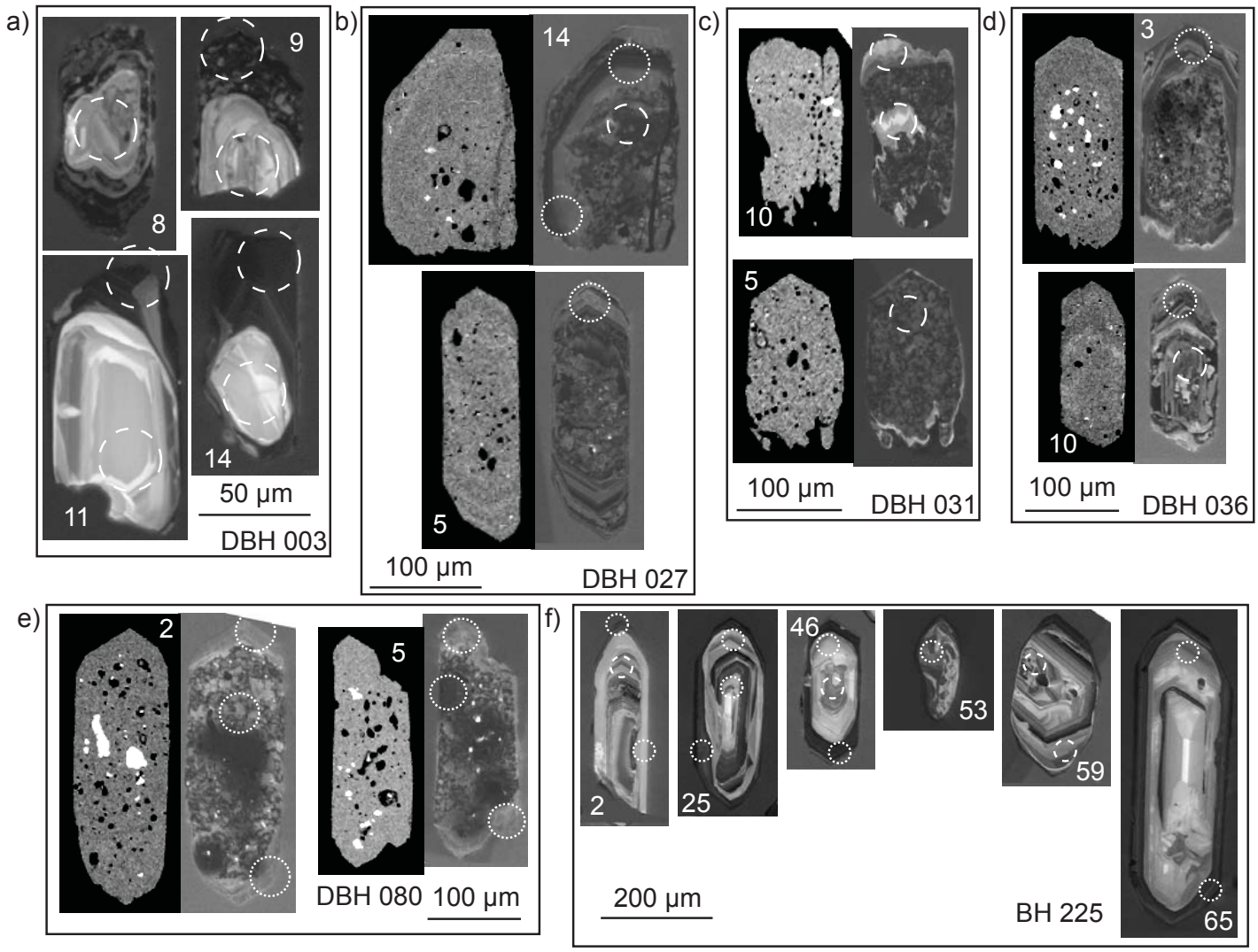

Figure B1, Kellett et al.